

Fast and Efficient Piezo-Photocatalytic Mineralization of Ibuprofen by BiOBr Nanosheets under Solar Light Irradiation

*Original*

Fast and Efficient Piezo-Photocatalytic Mineralization of Ibuprofen by BiOBr Nanosheets under Solar Light Irradiation / Falletta, Ermelinda; Galloni, Melissa G.; Mila, Nikoletta; bin Roslan, Muhammad N.; Abd Ghani, Noraini; Cerrato, Giuseppina; Giordana, Alessia; Magni, Mirko; Spriano, Silvia; Boffito, Daria C.; Bianchi, Claudia L.. - In: ACS PHOTONICS. - ISSN 2330-4022. - 10:11(2023), pp. 3929-3943. [10.1021/acsphotonics.3c00724]

*Availability:*

This version is available at: 11583/2985085 since: 2024-01-15T17:00:29Z

*Publisher:*

American Chemical Society

*Published*

DOI:10.1021/acsphotonics.3c00724

*Terms of use:*

This article is made available under terms and conditions as specified in the corresponding bibliographic description in the repository

*Publisher copyright*

(Article begins on next page)

# Fast and Efficient Piezo-Photocatalytic Mineralization of Ibuprofen by BiOBr Nanosheets under Solar Light Irradiation

Published as part of the ACS Photonics virtual special issue "Photonics for Energy".

Ermelinda Falletta,\*<sup>○</sup> Melissa G. Galloni, Nikoletta Mila, Muhammad N. bin Roslan, Noraini Abd Ghani, Giuseppina Cerrato, Alessia Giordana, Mirko Magni, Silvia Spriano, Daria C. Boffito, and Claudia L. Bianchi\*<sup>○</sup>



Cite This: ACS Photonics 2023, 10, 3929–3943



Read Online

ACCESS |



Metrics & More



Article Recommendations



Supporting Information

**ABSTRACT:** In the present work, the piezoelectric-like behavior of BiOBr nanosheets was utilized to suppress the recombination of photoexcited charges. The piezo-photocatalytic properties of an easily synthesized photocatalyst were tested for the degradation of ibuprofen, a nonsteroidal anti-inflammatory drug. Under ultrasound and solar light irradiation, the reaction rate for ibuprofen mineralization was found to be higher in the BiOBr nanosheets compared with those from the individual photocatalysis and piezocatalysis approaches, respectively. A percentage of synergy higher than 60% was calculated, resulting in the achievement of complete mineralization in less than 30 min. Based on the results, a possible piezo-photocatalytic mechanism, based on the separation of photoinduced charges and the formation of highly active radicals, has been proposed. Furthermore, various scavengers were used to identify the active species by trapping holes and radicals generated during the piezo-photocatalytic degradation process. The main transformation products formed during both photo- and piezo-photodegradation processes were identified by ultraperformance liquid chromatography–mass spectrometry (UPLC/MS), and the ibuprofen degradation pathway was proposed. The very promising results offer an advantageous approach to drug mineralization without the need for costly materials or expensive processes.

**KEYWORDS:** bismuth oxybromide, ibuprofen, ultrasound, photocatalysis, piezo-photocatalysis, mineralization



In recent years, water crisis and continuous contamination of water basins pose a serious threat to water resources and well-being of society.

Pharmaceutical and personal care products (PPCPs), steroids, and hormones are some of the pollutants already found in water.<sup>1</sup> Among the most well-known pharmaceuticals, nonsteroidal anti-inflammatory drugs (NSAIDs) are characterized by a broad scope of properties widely used in human and veterinary medicine. Ibuprofen (IBU) is an important exponent of NSAIDs. It is the third most popular, highly prescribed, and most marketed over-the-counter drug in the world,<sup>2</sup> with market size value at USD 90 million in 2022 and projected to reach USD 110.7 million by 2030.<sup>3</sup>

The rapid growth and aging of world population has caused a drastic increase in NSAID consumption, contributing to increasing drug concentrations in surface waters.<sup>4</sup>

In this context, because of the ever-increasing demand for fresh water caused by population growth, drought, and high consumption in the agricultural and industrial sectors, the possibility to reuse wastewater is a major challenge.<sup>5</sup>

However, traditional wastewater treatment plants (WWTPs) are generally not very effective in removing contaminants of emerging concern (CECs), such as PPCPs and their recalcitrant metabolites, due to their high chemical stability.

Regarding ibuprofen, it has been demonstrated that after ingestion, 15% of the drug leaves the body in unchanged form, 26% as metabolized hydroxyl-ibuprofen, and 43% as carboxy-ibuprofen;<sup>6</sup> both the latter forms have been found in untreated municipal wastewater as well as in hospital or industrial production waste.<sup>6,7</sup> Regarding the toxicity of ibuprofen and its metabolites, it has been properly documented, as well as its synergistic ecotoxicological effects when present in the mixture with other NSAIDs.<sup>2</sup>

**Received:** May 29, 2023

**Published:** October 20, 2023



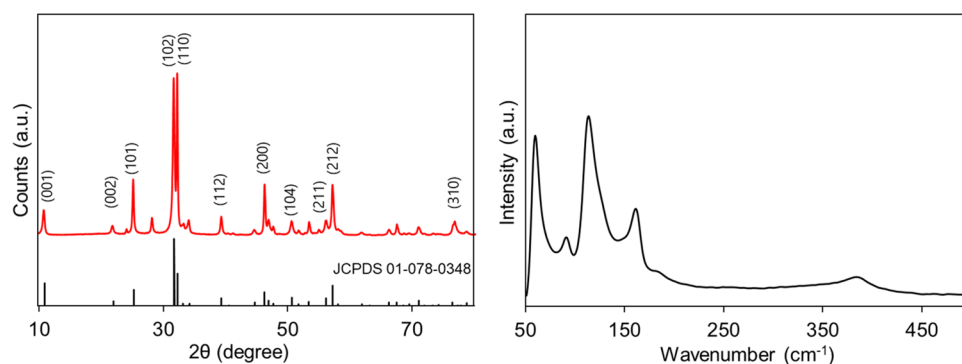


**Figure 1.** (a) XRPD pattern of BiOBr compared to the reference diffraction pattern (JCPDS 01–078–0348); (b) Raman spectrum of BiOBr.

In this scenario, researchers have invested their efforts in developing new methods for abatement of PPCPs from the environment. Among the different approaches, advanced oxidation processes (AOPs) offer effective alternatives. Heterogeneous photocatalysis represents an excellent example of AOPs using semiconductors and a source light to produce oxidants, such as hydroxyl ( $\text{OH}^\bullet$ ), peroxy ( $\text{O}_2^\bullet$ ), and hydroperoxide ( $\text{HO}_2^\bullet$ ) radicals, to mineralize organic contaminants to carbon dioxide and water.<sup>8</sup> By this approach, when the photocatalyst surface is properly irradiated and absorbs energy equal to or greater than the band gap, an electron is promoted from the valence band (VB) to the conduction band (CB), leading to an electron–hole pair, responsible for the production of radicals and promoting redox reactions.<sup>9</sup>

The photocatalytic degradation of IBU has been already investigated using  $\text{TiO}_2$  under ultraviolet (UV) irradiation,<sup>10–13</sup> but few data are reported on the  $\text{TiO}_2$  mineralization capacity, and they demonstrated the greater toxicity of the metabolites compared to ibuprofen.<sup>10</sup> In this context, the effect of gold nanoparticle incorporation on the  $\text{TiO}_2$  surface has also been investigated, demonstrating that the presence of noble metal nanoparticles causes a stronger absorption in the visible-light region due to their surface resonance plasmon band, leading to almost full ibuprofen degradation within 60 min, although only 24% is mineralized at the same time.<sup>14</sup> In addition, the potentialities of other candidate photocatalysts have been explored. By way of example, bimetallic copper–iron  $\text{ZrO}_2$ , prepared by incipient wetness impregnation, has been recently tested for the IBU mineralization by a heterogeneous Fenton-like process,<sup>15</sup> achieving 83% mineralization under optimum conditions (from 200 to 400 mg/L catalyst dosage, 10 ppm IBU) within a wide range of pH (3–5).

More in general, so far, photocatalysis technology has not been used in practical applications because of the drastic limitation due to the fast photoinduced electron–hole recombination, leading to the produced charges diffusing to the photocatalyst surface strongly and reducing the photocatalytic activity.

Therefore, there is an urgent need to identify better performing photocatalysts that are capable of attaining a complete and fast mineralization of ibuprofen by sustainable approaches.

The combination of different techniques enhances the process efficiency, speeding up the degradation and contributing to the reduction of hazardous byproduct formation.<sup>4,16</sup> It has been demonstrated that ultrasound (US)-assisted photo-

catalysis positively affects the highly active radical species formation.<sup>17,18</sup>

In this regard, piezo-photocatalysis (piezoelectric-assisted photocatalysis) is an innovative strategy for pollutant degradation from wastewater by a proper photo-piezoelectric catalyst.<sup>19</sup> The mechanical energy (e.g., ultrasound vibrations) promotes electric charges at the surface of this type of photocatalysts, enhancing the photoinduced charge separation by the piezoelectric effect.<sup>20–22</sup> The free charges accumulated on the material surface promote redox reactions involved in the degradation of organic pollutants. Therefore, piezo-photocatalysts are able to convert mechanical energy at first to electrical energy and then to chemical energy.

Recently, Bi-based photocatalysts, in particular bismuth oxyhalides ( $\text{BiOX}$ , where  $\text{X} = \text{Cl}, \text{Br}, \text{or I}$ ), have received much attention because of the easy synthesis, high chemical stability, unique layer structure, and great lifetime of electric charges after light irradiation.<sup>23–26</sup> They are a class of very promising semiconductor photocatalysts characterized by layered structures consisting of interlacing  $[\text{Bi}_2\text{O}_2]$  slabs and double  $[\text{X}]$  slices.<sup>26–28</sup>

Like all photocatalytic semiconductors, under light irradiation,  $\text{BiOX}$  generate photoinduced hole–electron pairs and lead to the formation of reactive oxygen species (ROS).

However, the existence of an electric field between  $[\text{Bi}_2\text{O}_2]^{2+}$  and  $\text{Cl}^-$  layers guarantees that the photoproduct charges can be effectively separated.

Although, on the one hand, the photocatalytic properties of  $\text{BiOX}$ , especially  $\text{BiOCl}$  and  $\text{BiOBr}$ , have been fairly studied,<sup>29–32</sup> on the other hand, only few studies have addressed toward the piezo-enhanced photoactivity of this class of materials.<sup>19</sup>

Ismail et al. demonstrated the enhanced effect of US application in the rhodamine-B decomposition by  $\text{BiOCl}$  microspheres powders.<sup>33</sup> Besides, Lei and co-workers reported the extraordinary piezo-photoactivity of 2D  $\text{BiOBr}$  in the removal of organic dyes, obtaining the percentage of abatement 5.62 and 11.0 times higher than those obtained from the individual photocatalysis and piezocatalysis, respectively.<sup>16</sup>

Herein, we investigated the photo- and piezo-photocatalytic properties of  $\text{BiOBr}$  nanosheets in the degradation of ibuprofen in different water matrices (ultrapure and simulated drinking water) to evaluate the potential application of the piezo-photocatalyst in real environments. To the best of our knowledge, this is the first time that the synergistic effect between photo and piezo properties of  $\text{BiOBr}$  has been investigated for ibuprofen degradation. The photodegradation

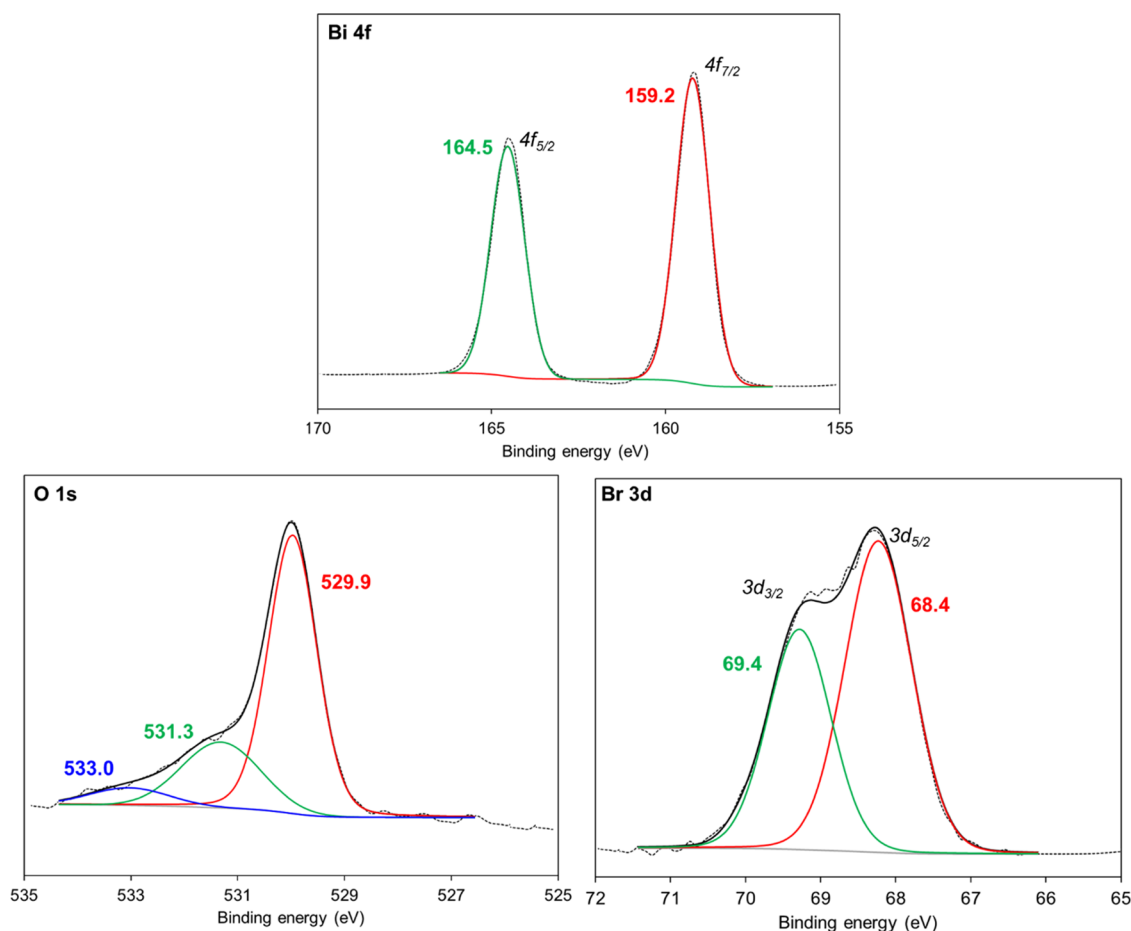


**Figure 2.** High-resolution (HR) XPS spectra of Bi 4f (a), O 1s (b), and Br 3d (c) for BiOBr. Deconvolutions in sub-bands and the resulting fitted spectra (black lines) are also reported.

kinetics of ibuprofen was properly investigated, and the active species involved in the degradation process were identified using proper scavengers by trapping holes and radicals.

Eventually, the transformation products (TPs) derived from the photo- and piezo-photodegradation processes were properly identified, and the ibuprofen degradation pathway was proposed.

## RESULTS AND DISCUSSION

**Catalyst Characterization.** BiOBr was synthesized by a facile solvothermal method. The X-ray diffraction (XRD) pattern of the obtained material (Figure 1a) exhibits intense and clear diffraction peaks, confirming the crystallinity of the as-prepared BiOBr sample. The main diffraction peaks at about 10.8, 21.8, 25.2, 31.7, 32.2, 39.3, 46.3, 50.7, 53.4, 57.2, and 76.8° can be indexed to the corresponding (001), (002), (101), (102), (110), (112), (200), (104), (211), (212), and (310) planes of the tetragonal BiOBr phase (JCPDS 01–078–0348). In addition, another peak at ca. 28° could be detected: It cannot be attributed to the typical BiOBr crystalline phase, but it could be ascribed to the presence of small traces of pure  $\alpha$ -Bi<sub>2</sub>O<sub>3</sub>, according to the standard JCPDS file n. 76–1730 corresponding to the monoclinic phase with a space group P21/c of bismuth oxide.<sup>34</sup>

Considering the symmetry in the crystal structure, six Raman active modes are theoretically expected: They are all observed for BiOBr, as evidenced in Figure 1b.<sup>35,36</sup> The most intense signal at 113 cm<sup>−1</sup> and the peak at 160 cm<sup>−1</sup> are

assigned to the A<sub>1g</sub> Bi–Br stretching modes. Besides, the B<sub>1g</sub> mode, related to the motion of the oxygen atom, gives a weak signal at 385 cm<sup>−1</sup>. The E<sub>g</sub> modes can be all observed at 60, 90, and 425 cm<sup>−1</sup>, respectively. The low intensity of the signal located at higher wavenumbers has been related to the asymmetric origin and the structural constraint. However, the Raman peaks are sharp, confirming the crystallinity of the synthesized BiOBr system. Moreover, the asymmetric shape of the peak located at 113 cm<sup>−1</sup> could be attributed to either the presence of defects or local distortion in the BiOBr structure.

The attenuated total reflectance-Fourier transform infrared (ATR-FT/IR) spectrum of the sample is reported in Figure S.1. The peak located at 515 cm<sup>−1</sup> corresponds to the Bi–O stretching vibration, whereas the band at 3530 cm<sup>−1</sup> is associated with the stretching vibrations of surface hydroxyl groups. The latter can be oxidized by photogenerated holes to hydroxyl radicals, and a surface rich of hydroxyl groups could thus enhance the photocatalytic activity, as also reported in a recent study.<sup>37</sup> Other bands are present in the spectral region 1600–950 cm<sup>−1</sup> as well: They can be related to residual nitrate groups, resulting from the synthetic procedure (this feature is also present in the Raman spectrum relative to the same sample, exhibiting a weak peak at ca. 940 cm<sup>−1</sup>, not reported for the sake of brevity).

Figure S.2 shows the photoluminescence spectrum of the synthesized material. The signal at around 420 nm is observed, analogous to the literature data.<sup>38</sup> This band corresponds to the band-edge emission and can be assigned to free e<sup>−</sup>–h<sup>+</sup>



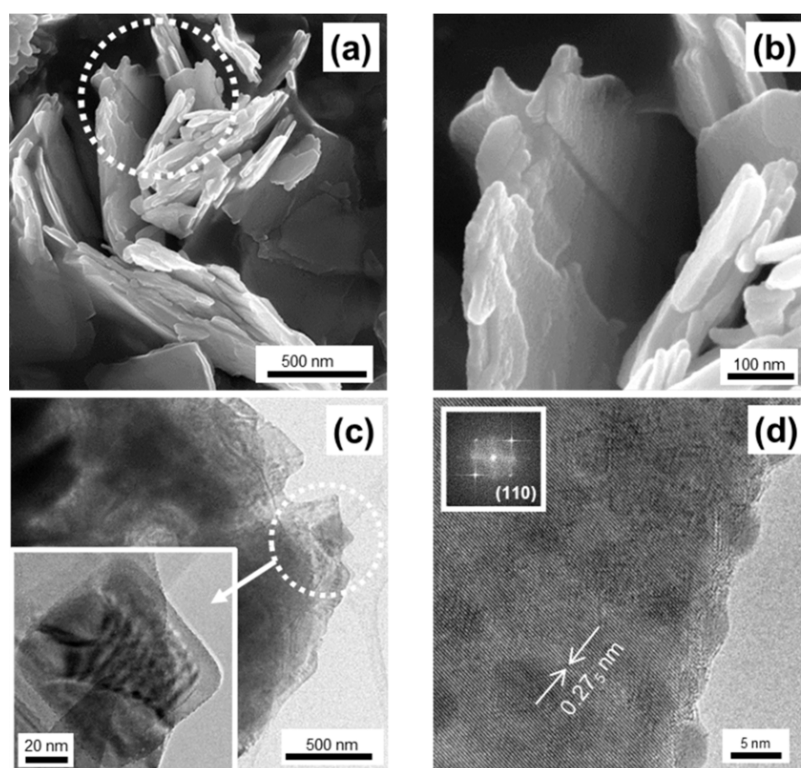


**Figure 3.** FESEM (a,b) and HRTEM (c,d) images of BiOBr.

recombination. The low intensity of the signal can be related to the lower recombination efficiency of  $e^-$  and  $h^+$ .

$N_2$  adsorption/desorption isotherm of BiOBr is reported in Figure S.3a: It exhibits a type IV isotherm according to the IUPAC classification. It is characteristic of a typical mesoporous material, as confirmed by the presence of a type H2 (de Boer classification) hysteresis,<sup>35,36</sup> described by mesopores with a diameter between 2 and 50 nm (Figure S.3b). Specifically, pore distribution showed that ca. 40–55% pores had a diameter between 2 and 5 nm, whereas ca. 10% was described by diameters lower than 2 nm (micropores). The BET specific surface area and pore volume of BiOBr correspond to 10 m<sup>2</sup>/g and 0.052 cm<sup>3</sup>/g.

The obtained results are in good agreement with the data reported in the scientific literature for similar systems,<sup>39,40</sup> demonstrating that this level of surface area and pore volume are sufficient to provide enough surface reaction sites and fast transfer channels that can more easily adsorb and transfer the pollutant through the structure and improve the photocatalytic activity.

BiOBr elemental composition was verified by X-ray photoelectron spectroscopy (XPS). The XPS survey spectrum (Figure S.4a) confirms the existence of Bi, O, and Br elements on the BiOBr surface without other prominent impurities. Figure 2 shows the high-resolution (HR) spectra of Bi 4f, O 1s, and Br 3d: They have been obtained by calibrating the binding energy values using the C 1s peak (at 284.6 eV) as the reference. The HR spectrum of the latter is shown in Figure S.4b. According to Jiang et al.,<sup>41</sup> it was fitted by three peaks at 289, 286.1, and 284.6 eV, respectively. In particular, the first two peaks (289 and 286.1 eV) were ascribable to the oxygen bound species C–O and C(O)O, whereas the third at 284.6 eV was related to elemental carbon. Regarding the HR XPS Bi 4f spectrum of BiOBr (Figure 2a), according to the literature,<sup>42</sup>

the two peaks at 164.5 and 159.2 eV, corresponding to Bi 4f<sub>5/2</sub> and Bi 4f<sub>7/2</sub>, indicate that in the BiOBr nanosheets bismuth was present as Bi<sup>3+</sup>. Regarding the HR XPS O 1s spectrum (Figure 2b), it can be deconvoluted into three peaks centered at 529.9, 531.3, and 533.0 eV, associated with the lattice oxygen, and the peaks at around 531.4 and 532.6 eV are ascribed to oxygen vacancies (OVs) and chemisorbed oxygen (hydroxyl), respectively.<sup>43</sup> As demonstrated by Cai et al.,<sup>43</sup> the formation of OVs is advantageous to capture the photo-generated electron producing  $\cdot O_2^-$ , as demonstrated below. Finally, the XPS spectrum of Br 3d (Figure 2c) exhibits two major peaks at 68.4 and 69.4 eV, ascribed to Br 3d<sub>5/2</sub> and Br 3d<sub>3/2</sub>, respectively.

The zero-point charge (ZPC) is one of the most important parameters to understand the behavior of the catalysts because it plays a key role in pollutant adsorption from the aqueous phase, which is the first step of the photodegradation process. At pH values below the ZPC, the catalyst surface is positively charged, attracting anions, whereas at pH values above the ZPC, the surface is negatively charged, attracting cations. At neutral or slightly alkaline pH, IBU is negatively charged ( $pK_a$  of 4.85). As shown in Figure S.5, the ZPC of BiOBr was found to be at pH 6.13. Therefore, under the reaction conditions, the IBU adsorption on the catalyst surface should not be much favored. However, as confirmed by the degradation tests, the exposed positive charges on the BiOBr surface, even if they were not the majority, were enough to guarantee pollutant abatement.

The optical properties of the sample were characterized by ultraviolet–visible (UV–vis) diffuse reflectance spectroscopy (Figure S.6a), wherein an absorption edge of 430 nm was observed for BiOBr, implying the possibility of utilizing sunlight on this catalyst to drive the photocatalytic reaction.

The band energy of the material was calculated using the Tauc plot (Figure S.6b) according to the following equation

$$\alpha h\nu = A(h\nu - E_g)^{n/2}$$

where  $\alpha$ ,  $h\nu$ ,  $A$ , and  $E_g$  are the absorption coefficient, incident photon energy, a constant, and energy of the band gap, respectively. Considering that BiOBr is a typical indirect band-gap semiconductor, the  $n$  value is 4. The band-gap value of BiOBr nanosheets was 2.63 eV, which is suitable for harvesting visible light.

Field emission scanning electron microscopic (FESEM) and high-resolution transmission electron microscopic (HRTEM) images (Figures 3 and S.7) at low magnification (Figure S.7A) exhibited an intermediate morphology between a flower-like shape and a plain intercalated lamellar one, made up of nanosheets (and in very few cases of nanorods as well); when observed at higher magnification (Figure 3a,b), the main features can be referred to as lamellar structures with irregular shape and size, in some cases more stuck with each other, whereas in some others relatively more dispersed (with a mean thickness of ca. 40 nm). As the nanosheets/nanorods are quite thin and transparent, HRTEM has been resorted to highlight the ultimate morphology of the particles: Figure 3c shows a low-to-mid magnification image obtained for the BiOBr material in which it is possible to observe that the lamellae are really thin and the presence of Moiré's fringes as well (see the dark parallel straight lines in the figure).

As these fringes are generated by crystalline planes of different particles positioned on top of each other, we pushed forward the magnification of the same portion of the sample (Figure 3d): The crystalline features are thus confirmed by the presence of fringes all over the investigated particle with distance  $d = 0.27(5)$  nm which is in very good agreement with the literature,<sup>43</sup> ascribable to the (110) crystal planes of tetragonal BiOBr. This assignment is further confirmed by the fast Fourier transform (FFT) calculation (simulating a selected area electron diffraction (SAED) analysis) carried out (Figure S.7B). Some more HRTEM investigations were carried out (with relevant FFT calculation, simulating an SAED analysis) and the obtained images are shown in Figure S.8A,B, in which the presence of the (110) crystal planes is confirmed (section a), besides the evidence of fringes with  $d = 0.81(3)$  nm again all over the investigated particle (section b), and corresponding to the (001) crystal planes (JCPDS 01–078–0348). The elemental analysis of the sample has been reported for further information and the corresponding images are shown in Figure S.8B–F in the form of energy-dispersive X-ray (EDX) mapping and spectrum as well, indicating homogeneous signals for Bi, O, and Br consistent with a uniform composition throughout the nanosheets. The presence of C is ascribable to the preparation of the sample for the FESEM investigation.

Semiconducting properties of BiOBr nanosheets were investigated through electrochemical impedance spectroscopy (EIS), with the material being drop-cast on an indium tin oxide (ITO) glass plate. The variation of the space charge capacity of BiOBr as a function of the applied potential was studied in dark condition and in a near-neutral blank electrolytic aqueous solution of 0.1 M Na<sub>2</sub>SO<sub>4</sub>. The related Mott–Schottky (M–S) plots are shown in Figure S.9. According to the literature, the positive slope of the straight lines indicates that the obtained material is an  $n$ -type semiconductor. Looking at the intercept with the  $x$ -axis of the straight line, the flat band potential ( $E_{fb}$ )

of BiOBr ranges between  $-0.050$  and  $-0.025$  V vs SCE, depending on the frequency chosen. These data are sufficiently in agreement with the studies that have reported  $E_{fb}$  values between  $-0.35$  and  $0.04$  V vs SCE for this type of material.<sup>44,45</sup> The variability of the literature data can be ascribed to practical aspects such as the electrode preparation method. Hence, in the present work, after drop casting on the ITO support, the semiconductor was not subjected to any calcination or thermal treatment.

It is commonly accepted that for many semiconductors, the conduction band is quite close ( $0$ – $0.2$  eV more negative) to the flat band potential.<sup>44</sup> If an average value of 100 meV is set, it is possible to estimate that the conduction band of the synthesized BiOBr has a potential ( $E_{cb}$ ) between  $-0.150$  and  $-0.125$  V vs SCE, which is not sufficient to generate  $\bullet\text{O}_2^-$  species ( $E(\text{O}_2/\bullet\text{O}_2^-) = -0.57$  V vs SCE). However, as reported in the literature<sup>41</sup> and demonstrated below, the presence of OVs overcomes this limitation. As mentioned above, the optical band gap ( $E_{gap}$ ) of the material is 2.63 eV, leading to an estimation of the valence band potential ( $E_{vb}$ ) of ca. 2.5 V vs SCE.

Considering the oxidation potential ( $E_{ox}$ ) of ibuprofen equal to ca. 1.6–1.7 V vs SCE (previous studies have reported the oxidation peak potentials of a chemically irreversible process in 0.1 H<sub>2</sub>SO<sub>4</sub> and in 1 M HClO<sub>4</sub>),<sup>44,46</sup> the photogenerated holes in BiOBr have sufficient driving force ( $\geq 800$  mV) to oxidize the organic pollutant and produce at same time a certain amount of  $\bullet\text{OH}$  radical species ( $E(\text{HO}^\bullet/\bullet\text{OH}) = +2.25$  V vs SCE) that can play a role in the IBU degradation. Based on these results, a detailed mechanism for ibuprofen degradation over BiOBr is proposed (Scheme S1).

To better elucidate the effects of light on the kinetics of the charge carriers in BiOBr nanosheets, transient photocurrent measurements, in the presence of chopped light, and EIS investigation, in the dark and under artificial solar light illumination, were also carried out. The results, which are in agreement with the data already present in the literature for this type of material, are shown in Figure S.10. First, potentiostatic EIS measurements of a BiOBr-modified ITO electrode were performed under both the dark and solar light irradiation to identify any variation in the electrochemical response of the system. The electrode was immersed in the above-mentioned blank electrolytic solution and anodically polarized at 0.9 V vs SCE, a potential that maximized the photocurrent generation (preliminary tests not shown). Thus, in selected conditions, the only oxidation reaction that can take place should be the evolution of O<sub>2</sub>. EIS plots (Figures S.10A,B) evidenced a quite complex behavior of the semiconducting film, with a multi time-constant response not easily resolved. Nonetheless, generally speaking, in the Nyquist plot the diameter of the semicircle represents the charge-transfer resistance of the electrode reaction. The smaller is the diameter, smaller is the charge-transfer resistance, and, as a consequence, faster is the kinetics of the redox reaction at the semiconductor–electrolyte interface. As shown in Figure S.10a, under light, the circle radius was slightly smaller, indicating an improved (i.e., faster) charge-transfer process at the BiOBr nanosheet interface attributable to the photogenerated holes in the valence band that have sufficient oxidizing power to react with water molecules (see M–S analysis). The quite limited difference between dark and light conditions can be attributed, at least in part, to the well-known sluggish kinetics of water oxidation reaction that makes water

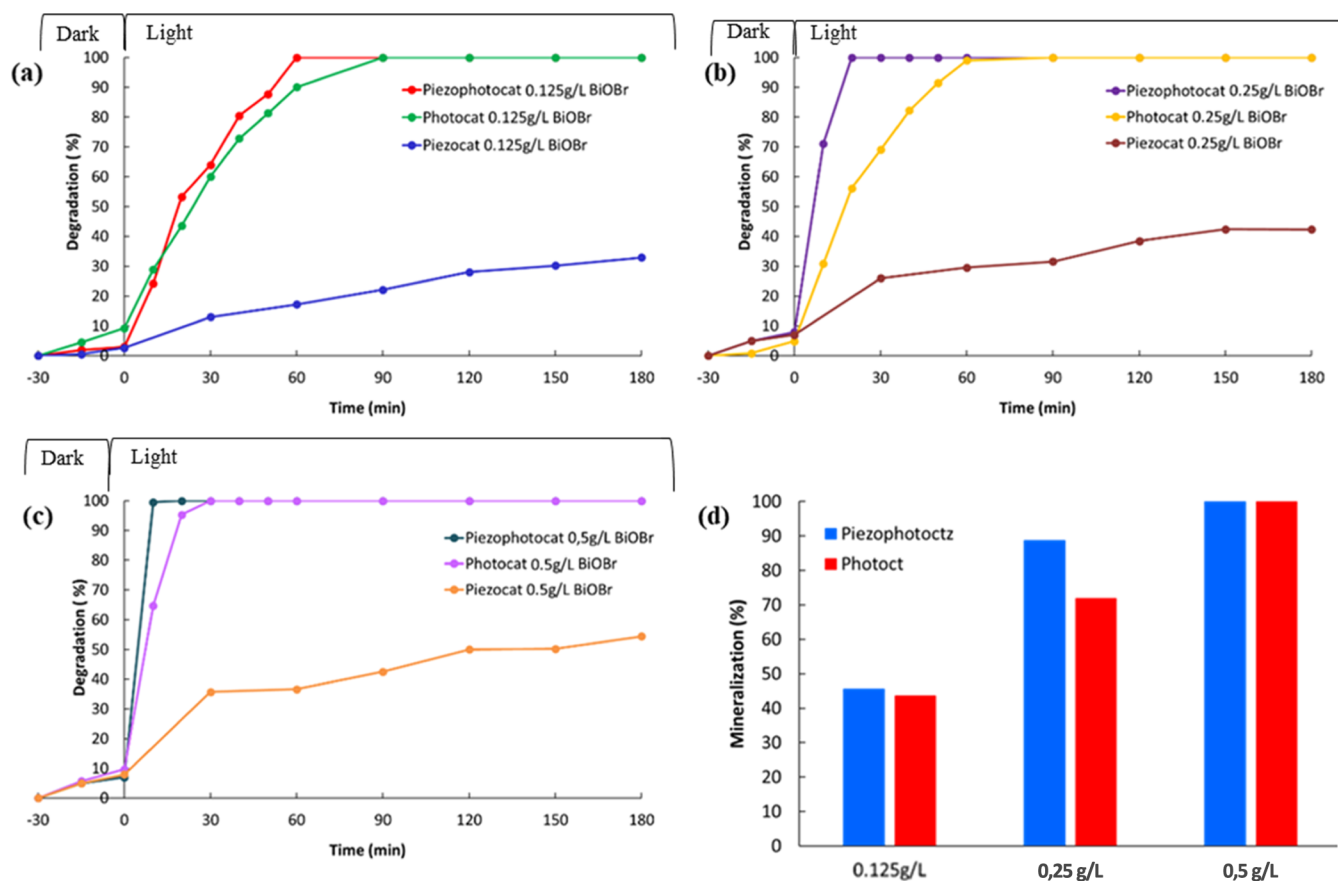


**Figure 4.** (a–c) Catalytic efficiency of BiOBr nanosheets in the photo-, piezo-, and piezo-photodegradation of IBU in UW. IBU concentration = 50 mg/L. (d) Percentage of mineralization of IBU during photo- and piezo-photodegradation processes (at the end of the degradation process).

molecules an inefficient hole scavenger, resulting in a fast electron–hole recombination within the semiconductor.

As shown in Figure S.10c, the synthesized sample exhibits a reproducible and relatively fast photocurrent response when irradiated. The background dark current versus photocurrent was monitored alternating dark and light conditions while polarizing the electrode at 0.9 V vs SCE. As expected, the anodic current sharply increases under light indicating photocurrent generation by BiOBr that acts as an n-type semiconductor, coherently with the Mott–Schottky analysis. The photocurrent density was at about 40 nA/cm<sup>2</sup> (calculated using the last two cycles, for which the light current easily reaches a stable value). The relatively low values of both dark current density and photocurrent density, with respect to literature analogues, are coherent with the quite high impedance values recorded through EIS and with the small differences between the EIS spectra in the dark and under light irradiation, respectively. These results can be attributable to the intrinsic electron–hole recombination process of the material and/or to the morphological features of the drop-casted film (e.g., active surface) that can reduce, for example, the charge-carrier transport within the matrix resulting in a more efficient charge recombination.

**Ibuprofen Abatement Tests.** The catalytic performances of the synthesized BiOBr nanosheets were evaluated in the degradation of IBU in different water matrices (ultrapure, UW, and simulated drinking water, DW) under solar light irradiation via photocatalysis, piezocatalysis, and coupling photocatalysis and piezocatalysis technologies (piezo-photo-

catalysis). The obtained results are discussed in the following sections.

**Effect of Catalyst Dose.** As reported in the literature,<sup>47,48</sup> photocatalysis is a catalyst mass-dependent reaction. Therefore, the effect of the catalyst dosage was investigated in the beginning (Figure 4a–c).

Before starting each test, the reaction mixture was maintained under stirring in the dark for 30 min until the adsorption/desorption equilibrium was reached to prevent adsorption effects in photocatalytic investigations. According to the ZPC results, a certain adsorption capacity of the photocatalyst was observed. However, the maximum adsorption capacity was always below 10%, demonstrating that this step did not significantly interfere with the results of the photocatalytic and piezo-photocatalytic reactions. Moreover, an additional 3 h adsorption study in dark conditions definitely confirmed that BiOBr nanosheets do not act as adsorbents (Figure S.11).

In the absence of a catalyst, ultrasound, light irradiation, and their combination were not able to degrade IBU (Figure S.12). Comparing the results obtained from the experiments based on the two catalytic approaches (photocatalysis and piezocatalysis), it is worth noting that BiOBr exhibited higher catalytic efficiency as a photocatalyst than as a piezocatalyst. However, by the coupling of the two techniques (piezo-photocatalysis), extraordinary results were obtained, leading to the complete IBU degradation in less than 30 min (Figure 4b,c). It is thus evident that the photocatalytic tests that lead to the complete IBU degradation are catalyst dose dependent.



In fact, it is known that large amounts of photocatalyst promote large amounts of ROS, even though an excess amount could reduce the catalytic activity because of an increase in the solution turbidity that reduces the absorption of the energy from light radiation.

In general, it is possible to observe that the IBU degradation by the photocatalytic process increased with the increase of catalyst concentration from 0.125 to 0.5 g/L. The enhanced degradation efficiency can be related to the presence of more active sites on the catalyst surface, promoting the production of more ROS during the degradation reaction. In contrast, the piezocatalytic method did not seem to be particularly affected by the catalyst dose.

However, low BiOBr dosage (0.125 g/L) was not adequate to promote a fast IBU degradation, not even combining piezocatalysis and photocatalysis because of the reduced catalytic surface available.<sup>49,50</sup>

The kinetics of the three diverse processes (photocatalysis, piezocatalysis, and piezo-photocatalysis) was determined by a pseudo-first-order kinetic model. The corresponding plots (Figure S.13) confirm the synergistic effect of the coupling of the two techniques with respect to the single ones.

By the kinetic constants ( $k$ ) of the different processes, the synergistic effect of the piezo- and photocatalysis combination was evaluated.

More in detail, the synergy factor and % synergy were calculated by the following equations<sup>50</sup> and the results are reported in Table 1.

$$\text{synergy factor} = \frac{k_{\text{piezophotocatalysis}}}{k_{\text{piezocatalysis}} + k_{\text{photocatalysis}}}$$

$$\% \text{synergy} = \frac{k_{\text{piezophotocatalysis}} - (k_{\text{piezocatalysis}} + k_{\text{photocatalysis}})}{k_{\text{piezocatalysis}} + k_{\text{photocatalysis}}} \times 100\%$$

**Table 1. Piezocatalytic, Photocatalytic, and Piezo-Photocatalytic Removal (%) of IBU (50 mg/L) after 20 min of Treatment, Synergy Factor, and % Synergy for IBU (50 mg/L) Degradation Carried Out with Different Catalyst Doses**

catalyst dose (g/L)	piezocat removal (%)	photocat removal (%)	piezophotocat removal (%)	synergy factor	% synergy
0.125	12	29	56	1.00	0.95
0.25	22	56	100	1.94	48.34
0.50	31	95	100	2.51	60.17

In accordance with the above data, for low catalyst dosage (0.125 g/L) no synergistic effect was observed due to the reduced catalytic surface available. In contrast, for higher catalyst concentrations, the synergy factor and % synergy were 1.94 and 2.51, or 48.34 and 60.17%, respectively. To better demonstrate the synergistic effect of the piezo-photocatalytic process, the kinetic constants of the combined approach were compared with those of the single processes and the results (Figure S.14) proved once more that the  $k$  values of piezo-photocatalytic reactions were higher than the sum of those obtained for the individual processes.

Figure 4d shows the degradation test results in terms of the IBU mineralization degree. The results clearly show the high

efficiency of BiOBr nanosheets in the mineralization process. In fact, already at low concentration (0.125 g/L) the catalyst showed a good mineralization efficiency (ca. 45), which reaches 100% by increasing the BiOBr content up to 0.50 g/L. The data collected for the reactions carried out with 0.25 g/L catalyst dose also clearly highlighted an important synergistic effect in the mineralization process and demonstrate that the mineralization process was fast (Figure S.15), reaching more than 60% final mineralization value after 30 min.

The stability of the synthesized nanostructures was further evaluated by reusing the piezo-photocatalyst. Because of the low amount of catalyst used for each test, the material was reused only once, maintaining very high activity even during the second test (Figure S.16). Moreover, the structural investigation of the material after the second test confirmed its stability (Figure S.17).

The scientific literature reports some data regarding IBU mineralization by TiO<sub>2</sub>-based photocatalysts under UV light.<sup>51–53</sup> However, little or nothing is reported regarding the BiOBr efficiency,<sup>16,30</sup> and data are always lower than those reported here to the best of our knowledge.

Li et al. recently critically investigated the selection of a proper synthetic approach for preparing piezoelectric BiOBr nanosheets, exhaustively reporting their piezo- and photoelectric properties.<sup>54</sup> More in detail, they optimized a hydrothermal route that assures the formation of BiOBr micro-nanosheets, exclusively using bismuth nitrate and potassium bromide as precursors, without the addition of a templating agent (i.e., ethylene glycol). Specifically, they demonstrated that the latter provides strongly aggregated particle size with low photoelectrochemical response. According to these premises, in the present study, a very simple strategy from the same precursors carried out under mild conditions was used.

Hu et al. and Lei and co-workers explored the piezo-photocatalytic activities of BiOBr and Au-decorated BiOBr nanoplates, respectively.<sup>16,55</sup> However, although the synthesized materials were similar to those reported here in terms of physicochemical characteristics and were applied for the degradation of organic molecules, the experimental conditions employed are very different and not comparable. Nevertheless, the strong piezo-photocatalytic properties of the material are always demonstrated. More in detail, Hu et al. addressed their attention on the degradation of carbamazepine by coupling visible-light irradiation and ultrasonication. Under these conditions, BiOBr nanoflakes showed very low photocatalytic activity. Only the US application permitted good pollutant degradation. Similarly, the material synthesized by Lei and co-workers reached a high level of rhodamine degradation only under piezo-photocatalytic conditions, whereas the results obtained only under visible-light irradiation were poor, when compared to those reported here. It is worth pointing out that a real comparison is not possible because the reaction conditions employed were very different.

However, the obtained results demonstrate that the coupling of piezocatalysis with photocatalysis is a very promising approach to mineralize IBU by a fast photocatalyst synthesized without the use of costly materials (e.g., doped catalysts with expensive metals or materials synthesized by complicated approaches).

**Synergistic Piezo-Photocatalytic Degradation Mechanism.** The physical mechanism of piezo-enhanced photodegradation for IBU decomposition is depicted in Figure 5.



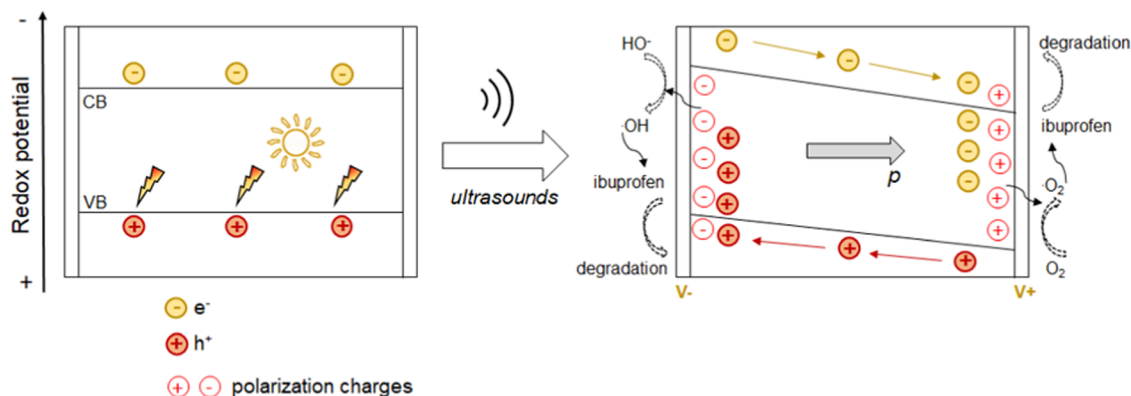


Figure 5. Piezo-enhanced photocatalytic mechanism of BiOBr nanosheets for IBU degradation.

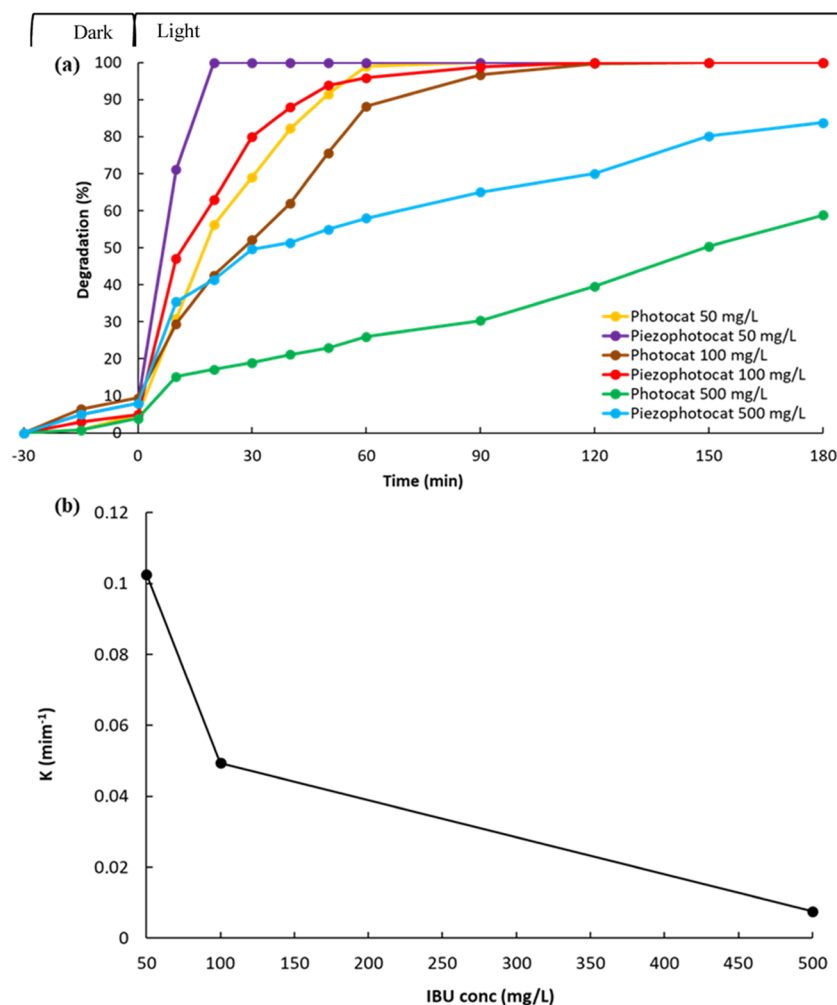


Figure 6. (a) Photo- and piezo-photodegradation of IBU at different initial concentrations by BiOBr nanosheets (0.25 g/L); (b) plot of kinetic constant values versus IBU concentration (mg/L).

When BiOBr is irradiated by solar light, the electrons in the valence band (VB) are promoted to the conduction band (CB), forming electron–hole pairs. The photoinduced carriers diffuse to the catalyst surface taking part in the chemical reaction and further produce some active radical species, such as  $\cdot\text{OH}$  and  $\cdot\text{O}_2^-$ . However, when an external strain is applied (US), an internal electric field is generated, causing a polarization, that reduces the recombination rate of the photogenerated carriers, enhancing the charge separation

efficiency. Consequently, a larger number of photoelectrons and holes are available for IBU oxidation.

**Effect of Initial Ibuprofen Concentration.** The effect of the initial IBU concentration on the BiOBr piezo-photoactivity was studied (Figure 6a,b).

In general, the increase in the initial IBU concentration caused a gradual reduction in the degradation efficiency of the catalyst in both approaches (photocatalysis and piezo-photocatalysis). In fact, as the initial IBU concentration increased,

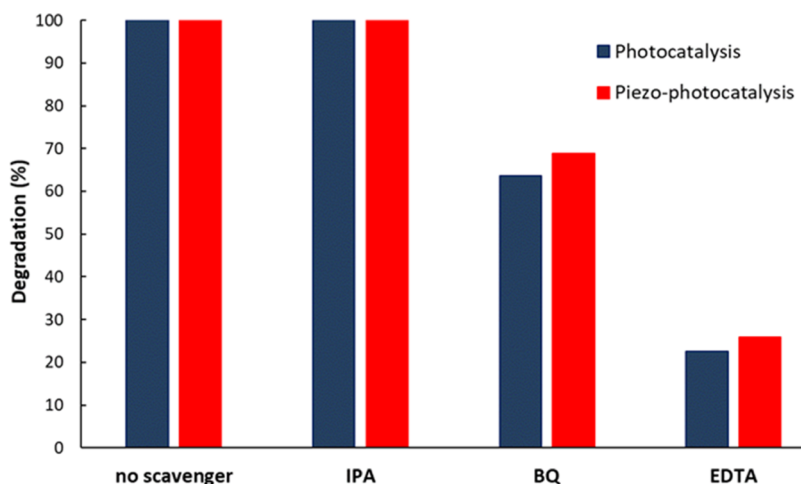
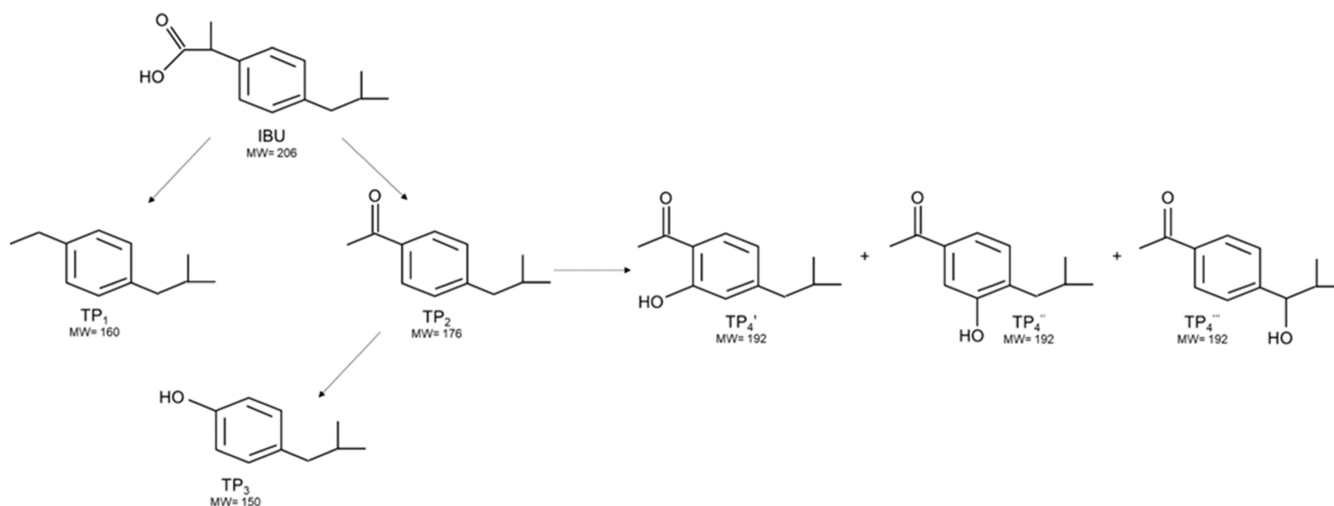


Figure 7. Effect of scavengers on the photo- and piezo-photodegradation of IBU (50 mg/L) by BiOBr (0.25g/L).

#### Scheme 1. IBU Degradation Pathway



the drug molecules were adsorbed on the catalyst surface, reducing the number of active sites on the BiOBr surface. At the same time, a larger amount of hydroxyl radicals were required for its degradation. However, the formation of hydroxyl radicals on the catalyst surface remained constant for a given light intensity, catalyst dose, and irradiation time. Consequently, the hydroxyl radicals produced were insufficient for IBU degradation when the drug concentration overcame a proper value. However, the coupled approach guarantees higher performances of the catalytic nanosheets, as described above and shown in Figure 6a. In fact, thanks to the piezoelectric behavior of the catalyst, the US application led to a polarization of the charges in the material, reducing the recombination rate of the photogenerated carriers with a positive effect on the catalyst activity. At the same time, US guaranteed a continuous surface catalyst regeneration, contributing to ROS generation.

**Effect of Initial pH.** To evaluate the effect of the pH conditions on the photoactivity of BiOBr nanosheets, the adsorption and piezo-photocatalytic investigations were extended to two extreme pH levels (pH 3 and 12). As shown in Figure S.18a, the pH of the solution slightly affects the adsorption capability of BiOBr. As reported in Figure S.5, at pH values above 6.13 (ZPC), the catalyst surface is

negatively charged. This means that under alkaline conditions IBU is completely deprotonated and, as a consequence, negatively charged. Therefore, repulsions between the IBU molecules and the BiOBr surface prevail, reducing adsorption phenomena, as well as the photocatalytic activity of the material. However, although the photocatalytic results of BiOBr at pH 3 were very similar to those obtained at spontaneous pH, the percentage of mineralization was 90% (Figure S.18b): a little bit lower than the results achieved by carrying out the reaction at spontaneous pH.

**Reactive Species Trapping Experiments.** To understand the role of the different photogenerated species produced during the photo- and piezo-photodegradation reactions, including  $h^+$ ,  $OH^-$ , and  $O_2^-$ , proper reactive species trapping experiments were carried out during IBU degradation processes. Disodium ethylenediaminetetraacetic acid (EDTA), *p*-benzoquinone (BQ), and isopropyl alcohol (IPA) were employed to trap  $h^+$ ,  $OH^-$ , and  $O_2^-$  scavengers, respectively. For both applied degradation technologies, similar results were obtained (Figure 7). The addition of EDTA (a  $h^+$  scavenger) had a strong effect in the IBU degradation, suggesting that  $h^+$  photogenerated charge carriers were those mainly involved in the photodegradation pathway. The addition of BQ (an  $O_2^-$  scavenger) slightly reduced the IBU degradation, indicating

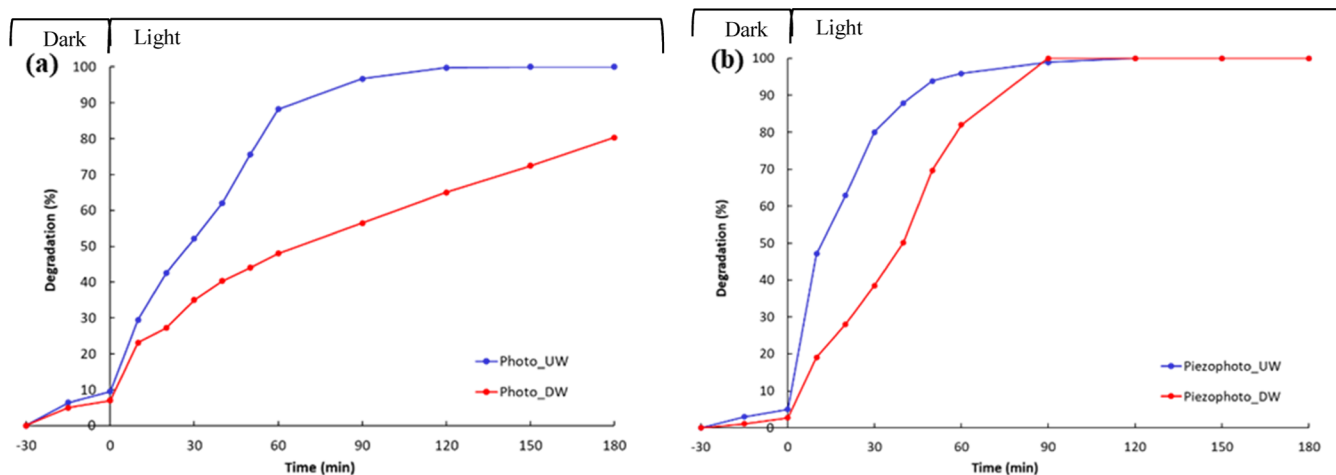


**Figure 8.** Comparison of the degradation percentage of IBU in UW and DW by photodegradation (a) and piezo-photodegradation (b). IBU concentration = 100 mg/L, ctz concentration = 0.25 g/L.

that  $\cdot\text{O}_2^-$ , generated by the presence of OV in BiOBr nanosheets, played only a minor role. In contrast, the  $\cdot\text{OH}^-$  scavenger seemed not to participate in the photodegradation process, based on the results obtained after the addition of IPA.

**Proposal of Ibuprofen Degradation Mechanism.** The produced TPs during the IBU degradation via both photo- and piezo-photocatalytic approaches were detected by ultra-performance liquid chromatography–mass spectrometry (UPLC/MS) analyses. Based on the identified intermediates, the supposed IBU degradation pathway is shown in Scheme 1, whereas the time profiles of all of the identified TPs, obtained by plotting the peak area of each selected TP versus the reaction time, are shown in Figure S.19. Decarboxylation, oxidation, and hydroxylation seemed to be the main processes involved in the IBU degradation.

The decarboxylation of the side chain of IBU can be attributed to the  $\text{h}^+$  attack, leading to  $\text{TP}_1$ , whereas for the formation of  $\text{TP}_2$  a subsequent oxidation reaction was required.<sup>29</sup> A radical attack ( $\text{HO}_2\cdot$ ) was responsible for  $\text{TP}_3$ .<sup>56</sup> Finally, the hydroxylated species ( $\text{TP}_{192}$ ) resulted from the reaction of  $\text{TP}_2$  with  $\cdot\text{OH}^-$ .

Although, on the one hand, the same TPs were recognized during both degradation procedures, on the other hand, differences were observed in their time profiles (Figure S.19). Most part of the TPs showed a bell shape trend and only a few byproducts exhibited an increasing concentration. The major difference concerned the formation and degradation of  $\text{TP}_2$  that during the piezo-photodegradation process was converted faster into other further hydroxylated products that were subsequently degraded (Figures S.19b,c).

**Effect of Water Matrix Composition.** To test the effect of the water matrix composition on the photocatalytic activity of the synthesized BiOBr nanosheets, the IBU photo- and piezo-photodegradation reactions were carried out in simulated drinking water (DW, Figure 8).

It is worth noting that during both degradation processes, the catalyst activity was strongly affected by the environment. The results showed that an increase in the ionic strength value seemed to have a negative effect on the catalyst, slowing its activity. In fact, the electrolytes can compete with the IBU molecules for adsorption on the active sites. However, the application of US during the photocatalytic process alleviated

the effect of inorganic ions in solution, ensuring a continuous and rapid regeneration of the catalyst surface, leading to complete IBU degradation in both UW and DW after 90 min treatment.

As shown in Figure S.20, during both degradation approaches in the two different environments (UW and DW), the same TPs reported in Scheme 1 were identified. However, based on the obtained results, the effect of the environment on the degradation of the main TP ( $\text{TP}_2$ ), whose degradation was only slowed down during the piezo-photocatalytic process, whereas was completely inhibited when US is not applied. This finding can be directly related to the effect of electrolytes described above which was the competition between IBU molecules and inorganic ions for the active sites of the catalyst. However, while  $\text{TP}_2$  was accumulated in solution during the established reaction time by the photocatalytic IBU degradation in DW, in contrast, it was gradually degraded by the piezo-photocatalytic process, albeit at a slower rate than that observed in UW.

## CONCLUSIONS

In summary, the BiOBr nanosheet photocatalyst was successfully synthesized and properly characterized. Its catalytic performance toward ibuprofen mineralization was enhanced by combining photocatalysis with the piezoelectric-like effect. The external strain applied using pulsed ultrasound induces an internal electric field in the nanosheets responsible for the piezoelectric-like effect, causing a polarization in the material that reduces the recombination rate of the photo-generated carriers enhancing the charge separation efficiency.

As a result, the synergistic effect of the coupling of photo- and piezocatalysis realized complete mineralization of the drug in less than 30 min. For the piezo-photocatalytic process, the reaction rate was 2.51 times the sum of the two single processes (photocatalysis and piezocatalysis). Moreover, it was demonstrated that the piezo-photocatalytic degradation of ibuprofen was mostly due to  $\text{h}^+$  photogenerated charge carriers, as indicated by radical trapping investigations.

The identification of the transformation products produced during the process demonstrated that decarboxylation, oxidation, and hydroxylation are the main processes involved in drug degradation.

In conclusion, this is the first application of BiOBr as a piezo-photocatalyst for ibuprofen degradation, to the best of our knowledge, and the obtained results were extraordinarily promising because they demonstrate that the ultrasonic application enhances the IBU degradation acting on different aspects: boosting charge separation, reducing particle aggregation, improving the availability of active sites, promoting mass transfer between the catalyst's surface and the solution reaction, and active radical formation.

The coupling of piezocatalysis with photocatalysis is a very interesting approach to exploit for wastewater treatment, not requiring the use of costly materials prepared by expensive procedures.

## METHODS

**Chemicals.** Glacial acetic acid ( $\text{CH}_3\text{COOH}$ ) and nitric acid ( $\text{HNO}_3$ ) were obtained from Carlo Erba, whereas other chemicals were purchased from Sigma-Aldrich. All chemicals were analytical grade and used as received without any further purification.

**Bismuth Oxybromide (BiOBr) Preparation.** 33 mL of 0.1 M KBr aqueous solution (3.3 mmol) was added dropwise to 55 mL of 0.1 M  $\text{Bi}(\text{NO}_3)_3 \cdot 5\text{H}_2\text{O}$  (5.5 mmol) aqueous solution 10 wt % in glacial acetic acid. The suspension was maintained at room temperature under vigorous magnetic stirring for 24 h. The as-obtained white powder (ca. 1 g) was recovered by filtration, washed with ultrapure water up to neutral pH, and dried overnight in air.

**BiOBr Characterization.** The crystal structure and phase composition were determined by X-ray powder diffraction (XRPD) using a PANalytical X'Pert PRO diffractometer ( $\text{Cu K}\alpha = 1.54060 \text{ \AA}$ ) equipped with an X-ray source operating at 40 kV  $\times$  40 mA. Before the analysis, the powder was finely ground and spread on an aluminum flat-plate horizontal sample holder. The diffractogram was collected in the  $10\text{--}80^\circ$  ( $2\theta$ ) range (step of  $0.02^\circ$   $2\theta$  and time for each step in 5–96 s intervals). The XRPD pattern was identified by comparison with the JCPDS files from the International Center for Diffraction Data Powder.

The chemical composition of BiOBr was analyzed by X-ray photoelectron spectroscopy (PHI 5000 Versaprobe II, ULVAC-PHI, Inc., Kanagawa, Japan) using an X-ray source (Al-K $\alpha$  radiation line). The takeoff angle was set at  $45^\circ$  for detecting photoelectrons to a depth of 1–5 nm from the surface. The binding energy of the obtained spectra was calibrated using the C 1s peak (at 284.6 eV) as the reference.

Raman spectrum was recorded on a Bruker Vertex 70 spectrophotometer equipped with the RAMII accessory and a Ge detector by exciting the sample with a Nd:YAG laser source (1064 nm) with a resolution of  $4 \text{ cm}^{-1}$ .

The ATR-FTIR spectrum of the sample was recorded by using a Bruker Vertex 70 spectrophotometer (Bruker, Billerica, MA) equipped with a Harrick MVP2 ATR cell (resolution  $4 \text{ cm}^{-1}$ ).

The photoluminescence at room temperature was measured on the solid sample using a Varian Cary Eclipse fluorescence spectrophotometer, exciting at 265 nm (slit ex = 20 nm, em = 20 nm).

UV–vis diffuse reflectance (UV-DR) spectrum was collected at room temperature in 200–800 nm intervals through a double-beam UV–vis–near-infrared (UV–vis–NIR) scanning spectrophotometer (PerkinElmer Lambda 750s UV–vis spectrophotometer, PerkinElmer, Waltham, MA) equipped

with an integrating sphere assembly to evaluate the light absorbance properties of the sample. The powder sample was finely ground, uniformly pressed in a circular disk (E.D., ca. 4 cm), and included in the sample holder. The latter was inserted in a special quartz cuvette and placed on the window of the integrating sphere for reflectance measurements. The spectrum was measured using  $\text{BaSO}_4$  as reference. The measured reflectance values ( $R\%$ ) were converted to absorbance (Abs, au) by the following equation

$$\text{abs} = \log(1/R/100)$$

Specific surface area and porosity were determined through  $\text{N}_2$  adsorption/desorption isotherms at  $-196^\circ \text{C}$  using an automatic analyzer (Micromeritics Tristar II 3020). Ca. 1 g of dried powder was outgassed at  $150^\circ \text{C}$  for 4 h under vacuum to remove water and other volatile organic compounds adsorbed on the surface. Specific surface area value was calculated by Brunauer–Emmet–Teller (BET) eq (2-parameters,  $0.05 < p/p^\circ < 0.3$ ), considering the cross-sectional area of ca.  $16.2 \text{ \AA}^2$  molecule $_{\text{N}_2}$ . Pore volume and size distribution (PSD) were determined by the Barrett–Joyner–Halenda (BJH) model from the desorption branch of the collected isotherm in the  $0.3\text{--}0.95 \text{ p/p}^\circ$  window.

The zero-point charge (ZPC) of BiOBr was determined according to the literature.<sup>57</sup> About 50 mg of sample powder was weighed and introduced in 20 mL of  $\text{NaNO}_3$  0.1 M solutions under stirring. The initial pH values ( $\text{pH}_{\text{initial}}$ ) of the solutions were adjusted by properly adding 0.1 M  $\text{HNO}_3$  or NaOH to drop in the 4.00–10.00 range. The suspensions were maintained under stirring (250 rpm). After 24 h, the suspensions were centrifuged (3000 rpm for 10 min), and the final pH values ( $\text{pH}_{\text{final}}$ ) were measured. By plotting the difference between the  $\text{pH}_{\text{final}}$  and  $\text{pH}_{\text{initial}}$  ( $\Delta\text{pH}$ ) as a function of the  $\text{pH}_{\text{initial}}$ , we determined  $\text{pH}_{\text{pzc}}$  as the intersection of the resulting line at which  $\Delta\text{pH} = 0$ .

An electrochemical workstation (Autolab PGSTAT204, Metrohm) with a three-electrode system was used for the electrochemical measurements in the dark and under solar light illumination. The three electrodes consist of a platinum wire as a counter electrode, a calomel reference electrode, and a working electrode. The latter was prepared similarly to ref 57. 10 mg BiOBr was dissolved in 400  $\mu\text{L}$  acetone, forming a homogeneous suspension.<sup>58</sup> Then, 20  $\mu\text{L}$  of the as-produced sample was deposited on a slice of ITO glass ( $50 \times 50 \text{ mm}^2$ ) and dried at  $60^\circ \text{C}$  overnight. The electrolyte used was 0.1 M  $\text{Na}_2\text{SO}_4$ . The light source used for the experiments under solar irradiation and the light source used in the photocatalytic measurements were the same ( $35 \text{ W/m}^2$ ).

BiOBr morphology and elemental analyses were evaluated using a scanning electron microscope operating with a field emission source, model TESCAN S9000G, (Overcoached, Germany) with a source of Schottky type FEG; resolution: 0.7 nm at 15 keV (in In-Beam SE mode) and equipped with EDS Oxford Ultim Max (operated with Aztec software 6.0). The sample was supported on metallic stabs with C tape and then coated with Cr by means of ion-sputtering technique to improve the conductivity of the materials. To further investigate the ultimate morphology of the sample, HRTEM investigations were carried out and images were obtained by means of a JEOL JEM 3010 transmission electron microscope, operating at 300 kV and equipped with a LaB6 filament. The sample was dispersed onto Cu grids coated with amorphous carbon without any further treatment.



**Ibuprofen (IBU) Degradation Tests.** Three different types of tests were performed: piezocatalytic tests (labeled as piezocat), performed using sonication in the presence of BiOBr without light irradiation; photocatalytic tests under solar light irradiation (labeled as photocat), carried out in the presence of the photocatalyst; and piezo-photocatalytic degradation tests (labeled as piezophotocat), performed using simultaneous sonication and light irradiation in the presence of BiOBr.

Similar tests were also carried out in the absence of a catalyst to evaluate the contribution of photolysis (photo) as well as ultrasound (piezo) and their combination (piezophoto) in the IBU abatement. Experiments were carried out both in ultrapure water (UW) and simulated drinking water (DW), prepared as reported in Table S.1, according to the literature Annex B2 of the second protocol of the French Norm NF P41–650 regarding the specification for water filter pitchers.<sup>59</sup>

All tests were performed under atmospheric conditions in a 250 mL jacketed batch glass reactor maintained at constant temperature ( $24.0 \pm 0.1$  °C). The reactor was inserted into a homemade box with dark walls made of cloth. A lamp was installed above the reactor at a fixed height (25 cm). The radiation source was an ULTRA VITALUX 300W-OSRAM solar lamp with power density of irradiation of 35 W/m<sup>2</sup>.

A 20 kHz ultrasonic processor (VibraCell VCX 500, Sonics and Materials) equipped with a 13 mm tip composed of a titanium alloy (Ti-6Al-4 V) was located on the top of the reactor, and the US probe (136 mm) was immersed into the IBU solution. A pulsed sonication was adopted (5 s on/5 s off) and calibrated as reported by Pirola et al.<sup>60</sup> The ultrasound output power was 23 W.

Experiments were performed by stirring (250 rpm) a suspension composed of a proper amount of BiOBr powder and 100 mL of IBU solution at different concentrations (50–500 mg/L) in the dark for 30 min. Then, regarding the photocatalytic tests, the mixture was irradiated for 180 min, whereas for the piezocatalytic tests, pulsed sonication was applied for 180 min. Finally, for the piezo-photocatalytic experiments, both pulsed sonication and the light source were applied at the same time until the reaction ended. Tests were carried out at spontaneous pH depending on the type of water matrix used (ca. 7 in UW and 7.5 in DW). They were repeated 3 times to ensure reproducibility.

In addition, the piezocatalytic tests were also carried out at different pH conditions (pH 3 and pH 12), adjusting the acidity of the solutions and adding a proper amount of diluted HCl or NaOH.

To evaluate the adsorption properties of the synthesized material, three tests were carried out in UW at spontaneous pH (ca. 7), 3 and 12 with the IBU concentration of 50 mg/L and using 0.25 g/L catalyst, maintained under stirring in the solution for 3 h.

IBU abatement was monitored for a total of 210 min, sampling 2 mL aliquots every 15 min for the first 30 min and then every 30 min for the remaining 180 min. The collected aliquots were placed in 1.5 mL conical vials and centrifuged with a LaboGene ScanSpeed centrifuge at 13,500 rpm for 5 min before any analyses. The collected aliquots were quantitatively analyzed by a high-performance liquid chromatography/UV (HPLC/UV) instrument. The HPLC instrument (Agilent 1100 Series) was equipped with a C18 Supelco column (25 cm  $\times$  4 mm, 5  $\mu$ m), a 20  $\mu$ L injection loop, and a UV detector. Chromatographic analyses were performed with an isocratic elution of a mobile phase composed of 50% water,

50% acetonitrile, and 0.1% formic acid at 1 mL/min flow rate. The IBU disappearance and the related formation of byproducts were monitored at 230 and 260 nm, respectively. IBU abatement (%) was calculated according to

$$\text{IBU abatement (\%)} = \frac{C_0 - C_t}{C_0} \times 100\%$$

where  $C_0$  is the initial IBU concentration and  $C_t$  is the IBU concentration at time  $t$ .

A recycling test was carried out to demonstrate the reusability of the catalyst. More in detail, BiOBr nanosheets (catalyst dose: 0.25 g/L, IBU conc. = 50 mg/L; water matrix: UW) were subjected to a first piezocatalytic test. Then, at the end of the reaction, the catalyst was recovered by centrifugation and exposed to UV light irradiation for 2 h to remove any species adsorbed on its surface. Finally, it was reused for a second cycle of IBU piezo-photodegradation.

Tests in the presence of disodium ethylenediaminetetraacetate (EDTA), benzoquinone (BQ), and isopropyl alcohol (IPA) as scavengers for holes ( $h^+$ ), superoxide radical ( $\cdot O_2^-$ ), and hydroxyl radical ( $\cdot OH$ ), respectively, were carried out. They were realized under the following conditions: initial IBU concentration = 50 mg/L, catalyst concentration = 0.25 g/L, and scavenger amount = 3 mmol.

The effect of the catalyst dosage (from 0.125 to 0.500 g/L) and IBU concentration (50–500 mg/L range) was also investigated.

Total organic carbon (TOC) analyses were performed on the supernatant using a Shimadzu TOC-L analyzer to evaluate the mineralization capacity of the piezo-photocatalyst. TOC removal was computed according to

$$\text{mineralization capacity (\%)} = \frac{TOC_0 - TOC_t}{TOC_0} \times 100\%$$

where  $TOC_0$  is the initial TOC concentration, and  $TOC_t$  is the final one after 180 min irradiation.

Transformation products (TPs) were recognized by UPLC/MS analyses carried out on an LCQ Fleet ion trap mass spectrometer equipped with a UPLC UltiMate 3000 system containing a UV detector. A Zorbax RX-C18 (2.1  $\times$  150 mm, 5  $\mu$ m) column was maintained at 30 °C. The same chromatographic conditions used for the HPLC/UV were employed. The mass spectrometer was operated with electrospray ionization in both positive and negative ion modes. Full-scan mass spectra were recorded in the 50–1000 mass/charge ( $m/z$ ) range.

## ■ ASSOCIATED CONTENT

### Supporting Information

The Supporting Information is available free of charge at <https://pubs.acs.org/doi/10.1021/acsphotonics.3c00724>.

Electrolyte contents of the simulated drinking water (Table S.1); hypothesized mechanism of the solar light-induced photodegradation of IBU over BiOBr nanosheets (Scheme S1); ATR/FT-IR spectrum of BiOBr nanosheets (Figure S.1); PLS spectrum of BiOBr ( $\lambda_{\text{exc}}$  = 265 nm) (Figure S.2); characterization results of BiOBr: (a)  $N_2$  adsorption/desorption isotherms at  $-196$  °C; (b) pore size distribution (Figure S.3); survey spectrum for BiOBr (Figure S.4); point of zero charge of BiOBr (Figure S.5); (a) UV–vis absorption spectrum and (b) Tauc plot of BiOBr (Figure S.6); (A, B) HRTEM

images of different portions of the BiOBr sample: insets represent FFT calculations (simulating SAED analyses) on both portions (Figure S.7); (A) SEM image, (B–E) elemental mapping of Bi, Br, O, and C elements, respectively, (F) EDX spectrum of BiOBr (Figure S.8); Mott–Schottky plot depicting the variation of the capacity of space charge region (C) of the BiOBr film on an ITO electrode as a function of applied potential. Plots refer to three different frequencies (1 kHz, 100 and 10 Hz) and were derived by EIS spectra recorded in a blank solution (water +0.1 M Na<sub>2</sub>SO<sub>4</sub>) in the dark (Figure S.9); (a) Nyquist and (b) Bode plots of a BiOBr drop-casted film on the ITO electrode, recorded at 0.9 V vs SCE under artificial solar light irradiation and in the dark; (c) transient photocurrent response under the same potentiostatic polarization. Electrolyte: 0.1 M Na<sub>2</sub>SO<sub>4</sub> aqueous solution. When irradiated, front illumination setup was used (Figure S.10); adsorption investigation (IBU concentration: 50 mg/L; catalyst dose: 0.25 g/L; spontaneous pH) (Figure S.11); photo-, piezo-, and piezo-photodegradation of IBU (50 mg/L) in UW (Figure S.12); linear fittings of pseudo-first-order kinetics ( $a = 0.125 \text{ g/L BiOBr}$ ,  $b = 0.25 \text{ g/L BiOBr}$ ,  $c = 0.5 \text{ g/L BiOBr}$ ) (Figure S.13); synergistic effect of the piezo-photocatalytic degradation of IBU (Figure S.14); mineralization percentage of IBU (IBU conc. = 50 mg/L, BiOBr conc. = 0.25 g/L) (Figure S.15); reusability test of BiOBr nanosheets for IBU degradation (Figure S.16); XRD patterns of fresh and used BiOBr (Figure S.17); (a) adsorption and (b) piezo-photodegradation of IBU by BiOBr nanosheets (Figure S.18); time-resolved profiles of TPs of IBU (a), photo- (b) and piezo-photodegradation (IBU concentration 50 mg/L, ctz concentration 0.25 g/L, reaction time 180 min), (c) piezo-photodegradation (IBU concentration 50 mg/L, ctz concentration 0.25 g/L, reaction time 360 min) (Figure S.19); time-resolved profiles of TPs of IBU photodegradation in UW (a) and DW (b) and piezo-photodegradation in UW (c) and DW (d). IBU concentration 100 mg/L, ctz concentration 0.25 g/L, reaction time 180 min (Figure S.20) (PDF)

## AUTHOR INFORMATION

### Corresponding Authors

**Ermelinda Falletta** – Dipartimento di Chimica, Università degli Studi di Milano, 20133 Milano, Italy; Consorzio Interuniversitario Nazionale per la Scienza e Tecnologia dei Materiali (INSTM), 50121 Firenze, Italy; [orcid.org/0000-0002-3127-8967](https://orcid.org/0000-0002-3127-8967); Email: [ermelinda.falletta@unimi.it](mailto:ermelinda.falletta@unimi.it)

**Claudia L. Bianchi** – Dipartimento di Chimica, Università degli Studi di Milano, 20133 Milano, Italy; Consorzio Interuniversitario Nazionale per la Scienza e Tecnologia dei Materiali (INSTM), 50121 Firenze, Italy; [orcid.org/0000-0002-9702-6949](https://orcid.org/0000-0002-9702-6949); Email: [Claudia.bianchi@unimi.it](mailto:Claudia.bianchi@unimi.it)

### Authors

**Melissa G. Galloni** – Dipartimento di Chimica, Università degli Studi di Milano, 20133 Milano, Italy; Consorzio Interuniversitario Nazionale per la Scienza e Tecnologia dei Materiali (INSTM), 50121 Firenze, Italy

**Nikoletta Mila** – Dipartimento di Chimica, Università degli Studi di Milano, 20133 Milano, Italy; Consorzio

Interuniversitario Nazionale per la Scienza e Tecnologia dei Materiali (INSTM), 50121 Firenze, Italy

**Muhammad N. bin Roslan** – Department of Fundamental and Applied Sciences, Universiti Teknologi PETRONAS, 50603 Kuala Lumpur, Malaysia

**Noraini Abd Ghani** – Department of Fundamental and Applied Sciences, Universiti Teknologi PETRONAS, 50603 Kuala Lumpur, Malaysia

**Giuseppina Cerrato** – Dipartimento di Chimica, Università degli Studi di Torino, 10125 Torino, Italy; [orcid.org/0000-0001-8536-1398](https://orcid.org/0000-0001-8536-1398)

**Alessia Giordana** – Dipartimento di Chimica, Università degli Studi di Torino, 10125 Torino, Italy; [orcid.org/0000-0002-7566-6793](https://orcid.org/0000-0002-7566-6793)

**Mirko Magni** – Dipartimento di Scienze e Politiche Ambientali, Università degli Studi di Milano, 20133 Milano, Italy; [orcid.org/0000-0001-9776-2973](https://orcid.org/0000-0001-9776-2973)

**Silvia Spriano** – Dipartimento di Scienza Applicata e Tecnologia, Politecnico di Torino, 10129 Torino, Italy; [orcid.org/0000-0002-7367-9777](https://orcid.org/0000-0002-7367-9777)

**Daria C. Boffito** – Polytechnique Montr'éal, H3T 1J4 Montr'éal, Québec, Canada; [orcid.org/0000-0002-5252-5752](https://orcid.org/0000-0002-5252-5752)

Complete contact information is available at:

<https://pubs.acs.org/10.1021/acsphotonics.3c00724>

### Author Contributions

○E.F. and C.L.B. contributed equally to this work. E.F.: conceptualization, methodology, validation, supervision; writing—original draft, writing—review. M.G.G.: formal analysis, investigation, writing—original draft. N.M.: formal analysis. M.N.b.R.: formal analysis. N.A.G.: investigation. G.C.: investigation, data curation, writing—original draft. A.G.: investigation, data curation. M.M.: data curation. A.S.: investigation, data curation. DC.B.: writing—original draft, writing—review. C.L.B.: conceptualization, methodology, validation, supervision; Writing—original draft, writing—review, funding acquisition.

### Funding

Velux Stiftung Foundation is gratefully acknowledged for their financial support through the project 1381 “SUNFLOAT—Water decontamination by sunlight-driven floating photocatalytic systems”. This work was supported by the Department of Chemistry, Università degli Studi di Milano, Italy (Piano Sostegno alla Ricerca, PSR, grant 2022).

### Notes

The authors declare no competing financial interest.

## REFERENCES

- (1) Ellis, J. B. Pharmaceutical and personal care products (PPCPs) in urban receiving waters. *Environ. Pollut.* **2006**, *144* (1), 184–189, DOI: [10.1016/j.envpol.2005.12.018](https://doi.org/10.1016/j.envpol.2005.12.018).
- (2) Chopra, S.; Kumar, D. Ibuprofen as an emerging organic contaminant in environment, distribution and remediation. *Heliyon* **2020**, *6* (6), No. e04087.
- (3) Global Ibuprofen Market Size By Type (Tablet, Capsule), By Application (Rheumatoid Arthritis and Osteoarthritis, Cancer), By Geographic Scope And Forecast. <https://www.verifiedmarketresearch.com/product/ibuprofen-market/>.
- (4) Meroni, D.; Bianchi, C. L.; Boffito, D. C.; Cerrato, G.; Bruni, A.; Sartirana, M.; Falletta, E. Piezo-enhanced photocatalytic diclofenac mineralization over ZnO. *Ultrason. Sonochem.* **2021**, *75*, No. 105615.

- (5) Murgolo, S.; Franz, S.; Arab, H.; Bestetti, M.; Falletta, E.; Mascolo, G. Degradation of emerging organic pollutants in wastewater effluents by electrochemical photocatalysis on nanostructured  $\text{TiO}_2$  meshes. *Water Res.* **2019**, *164*, No. 114920.
- (6) Farré, M.; Asperger, D.; Kantiani, L.; González, S.; Petrovic, M.; Barceló, D. Assessment of the acute toxicity of triclosan and methyl triclosan in wastewater based on the bioluminescence inhibition of *Vibrio fischeri*. *Anal. Bioanal. Chem.* **2008**, *390*, No. 1999, DOI: 10.1007/s00216-007-1779-9.
- (7) Marković, M.; Jović, M.; Stanković, D.; Kovačević, V.; Roglić, G.; Gojgić-Cvijović, G.; Manojlović, D. Application of non-thermal plasma reactor and Fenton reaction for degradation of ibuprofen. *Sci. Total Environ.* **2015**, *505*, 1148–1155, DOI: 10.1016/j.scitotenv.2014.11.017.
- (8) Ma, D.; Yi, H.; Lai, C.; Liu, X.; Huo, X.; An, Z.; Li, L.; Fu, Y.; Li, B.; Zhang, M.; Qin, L.; Liu, S.; Yang, L. Critical review of advanced oxidation processes in organic wastewater treatment. *Chemosphere* **2021**, *275*, No. 130104.
- (9) Linsebigler, A. L.; Lu, G.; Yates, J. T. Photocatalysis on  $\text{TiO}_2$  Surfaces: Principles, Mechanisms, and Selected Results. *Chem. Rev.* **1995**, *95*, 735–758, DOI: 10.1021/cr00035a013.
- (10) da Silva, J. C. C.; Teodoro, J. A. R.; de Cássia Franco Afonso, R. J.; Aquino, S. F.; Augusti, R. Photolysis and photocatalysis of ibuprofen in aqueous medium: characterization of by-products via liquid chromatography coupled to high-resolution mass spectrometry and assessment of their toxicities against *Artemia Salina*. *J. Mass Spectrom.* **2014**, *49*, 145–153, DOI: 10.1002/jms.3320.
- (11) Achilleos, A.; Hapeshi, E.; Xekoukoulotakis, N. P.; Mantzavinos, D.; Fatta-Kassinos, D. UV-A and solar photo-degradation of ibuprofen and carbamazepine catalyzed by  $\text{TiO}_2$ . *Sep. Sci. Technol.* **2010**, *45*, 1564–1570, DOI: 10.1080/01496395.2010.487463.
- (12) Braz, F. S.; Silva, M. R. A.; Silva, F. S.; Andrade, S. J.; Fonseca, A. L.; Kondo, M. M. Photocatalytic degradation of ibuprofen using  $\text{TiO}_2$  and ecotoxicological assessment of degradation intermediates against *Daphnia similis*. *J. Environ. Prot.* **2014**, *5*, 620–626, DOI: 10.4236/jep.2014.57063.
- (13) Choina, J.; Kosslick, H.; Fischer, C.; Flechsig, G.-U.; Frunza, L.; Schulz, A. Photocatalytic decomposition of pharmaceutical ibuprofen pollutions in water over titania catalyst. *Appl. Catal., B* **2013**, *129*, 589–598, DOI: 10.1016/j.apcatb.2012.09.053.
- (14) Yao, X.; Hu, X.; Liu, Y.; Wang, X.; Wang, X.; Hong, X.; Hong, X.; Chen, X.; Chen, X.; Pillai, S. C.; Pillai, S. C.; Dionysiou, D. D.; Dionysiou, D. D.; Wang, D. Simultaneous photocatalytic degradation of ibuprofen and  $\text{H}_2$  evolution over Au/sheaf-like  $\text{TiO}_2$  mesocrystals. *Chemosphere* **2020**, *261*, No. 127759.
- (15) Hussain, S.; Aneggi, E.; Goi, D.; Trovarelli, A. Bimetallic Cu/Fe Catalysts for Ibuprofen Mineralization. *Catalysts* **2021**, *11* (11), No. 1383, DOI: 10.3390/catal11111383.
- (16) Lei, H.; Zhang, H.; Zou, Y.; Dong, X.; Jia, Y.; Wang, F. Synergetic photocatalysis/piezocatalysis of bismuth oxybromide for degradation of organic pollutants. *J. Alloys Compd.* **2019**, *809*, No. 151840.
- (17) Madhavan, J.; Grieser, F.; Ashokkumar, M. Combined advanced oxidation processes for the synergistic degradation of ibuprofen in aqueous environments. *J. Hazard. Mater.* **2010**, *178*, 202–208, DOI: 10.1016/j.jhazmat.2010.01.064.
- (18) Joseph, C. G.; Li Puma, G.; Bono, A.; Krishnaiah, D. Sonophotocatalysis in advanced oxidation process: a short review. *Ultrason. Sonochem.* **2009**, *16*, 583–589, DOI: 10.1016/j.ultsonch.2009.02.002.
- (19) Tu, S.; Guo, Y.; Zhang, Y.; Hu, C.; Zhang, T.; Ma, T.; Huang, H. Piezocatalysis and Piezo-Photocatalysis: Catalysts Classification and Modification Strategy, Reaction Mechanism, and Practical Application. *Adv. Funct. Mater.* **2020**, *30*, No. 2005158.
- (20) Hong, Y. T.; Ma, J. P.; Wu, Z.; Ying, J. S.; You, H. L.; Jia, Y. M. Piezo-electrochemical coupling of  $\text{AgNbO}_3$  piezoelectric nanomaterials. *Acta Phys. Sin.* **2018**, *67*, No. 107702, DOI: 10.7498/aps.67.20180287.
- (21) Starr, M. B.; Wang, X. Fundamental analysis of piezocatalysis process on the surfaces of strained piezoelectric materials. *Sci. Rep.* **2013**, *3*, No. 2160.
- (22) Sun, C.; Fu, Y.; Wang, Q.; Xing, L.; Liu, B.; Xue, X. Ultrafast piezo-photocatalytic degradation of organic pollutions by  $\text{Ag}_2\text{O}$ /tetrapod- $\text{ZnO}$  nanostructures under ultrasonic/UV exposure. *RSC Adv.* **2016**, *6*, 87446–87453, DOI: 10.1039/C6RA13464E.
- (23) Chen, L.; Yin, S.; Huang, R.; Zhou, Y.; Luo, S.; Au, C. Facile synthesis of  $\text{BiOCl}$  nano-flowers of narrow band gap and their visible-light-induced photocatalytic property. *Catal. Commun.* **2012**, *23*, 54–57, DOI: 10.1016/j.catcom.2012.03.001.
- (24) Hu, X.; Xu, Y.; Zhu, H.; Hua, F.; Zhu, S. Controllable hydrothermal synthesis of  $\text{BiOCl}$  nanoplates with high exposed {001} facets. *Mater. Sci. Semicond. Process.* **2016**, *41*, 12–16, DOI: 10.1016/j.mssp.2015.08.016.
- (25) Zhang, G.; Tan, Y.; Sun, Z.; Zheng, S. Synthesis of  $\text{BiOCl}/\text{TiO}_2$  heterostructure composites and their enhanced photocatalytic activity. *J. Environ. Chem. Eng.* **2017**, *5*, 1196–1204, DOI: 10.1016/j.jece.2017.01.040.
- (26) Galloni, M. G.; Ferrara, E.; Falletta, E.; Bianchi, C. L. Olive Mill Wastewater Remediation: From Conventional Approaches to Photocatalytic Processes by Easily Recoverable Materials. *Catalysts* **2022**, *12* (8), No. 923, DOI: 10.3390/catal12080923.
- (27) Di, J.; Xia, J. X.; Li, H. M.; Guo, S. J.; Dai, S. Bismuth oxyhalide layered materials for energy and environmental applications. *Nano Energy* **2017**, *41*, 172–192, DOI: 10.1016/j.nanoen.2017.09.008.
- (28) Cheng, H. F.; Huang, B. B.; Dai, Y. Engineering  $\text{BiOX}$  ( $\text{X}$  =  $\text{Cl}$ ,  $\text{Br}$ ,  $\text{I}$ ) nanostructures for highly efficient photocatalytic applications. *Nanoscale* **2014**, *6*, 2009–2026, DOI: 10.1039/c3nr05529a.
- (29) Arthur, R. B.; Bonin, J. L.; Ardill, L. P.; Rourke, E. J.; Patterson, H. H.; Stemmler, E. A. Photocatalytic degradation of ibuprofen over  $\text{BiOCl}$  nanosheets with identification of intermediates. *J. Hazard. Mater.* **2018**, *358*, 1–9, DOI: 10.1016/j.jhazmat.2018.06.018.
- (30) Liu, Y.; Hu, Z.; Yu, J. C. Photocatalytic degradation of ibuprofen on S-doped  $\text{BiOBr}$ . *Chemosphere* **2021**, *278*, No. 130376.
- (31) Lv, X.; Yuk Lam, F. L.; Hu, X. A Review on Bismuth Oxyhalide ( $\text{BiOX}$ ,  $\text{X}$  =  $\text{Cl}$ ,  $\text{Br}$ ,  $\text{I}$ ) Based Photocatalysts for Wastewater Remediation. *Front. Catal.* **2022**, *2*, No. 839072.
- (32) Yang, Y.; Zhang, C.; Lai, C.; Zeng, G.; Huang, D.; Cheng, M.; Wang, J.; Chen, F.; Zhou, C.; Xiong, W.  $\text{BiOX}$  ( $\text{X}$  =  $\text{Cl}$ ,  $\text{Br}$ ,  $\text{I}$ ) photocatalytic nanomaterials: Applications for fuels and environmental management. *Adv. Colloid Interface Sci.* **2018**, *254*, 76–93, DOI: 10.1016/j.cis.2018.03.004.
- (33) Ismail, M.; Wu, Z.; Zhang, L.; Ma, J.; Jia, Y.; Hu, Y.; Wang, Y. High-efficient synergy of piezocatalysis and photocatalysis in bismuth oxychloride nanomaterial for dye decomposition. *Chemosphere* **2019**, *228*, 212–218, DOI: 10.1016/j.chemosphere.2019.04.121.
- (34) Fatima, M. J.; Niveditha, C. V.; Sindhu, S.  $\alpha\text{-Bi}_2\text{O}_3$  photoanode in DSSC and study of the electrode–electrolyte interface. *RSC Adv.* **2015**, *5*, 78299–78305, DOI: 10.1039/c5ra12760b.
- (35) Zhang, D.; Li, J.; Wang, Q.; Wu, Q. High {001} facets dominated  $\text{BiOBr}$  lamellas: facile hydrolysis preparation and selective visible-light photocatalytic activity. *J. Mater. Chem. A* **2013**, *1*, 8622–8629, DOI: 10.1039/c3ta11390f.
- (36) Ferrer, M. M.; Rodrigues, J. E. F. S.; Almeida, M. A. P.; Moura, F.; Longo, E.; Pizani, P.; Sambrano, J. R. Theoretical methods for calculations of optical phonons in  $\text{BiOBr}$ : Analysis and correction of propagated errors. *J. Raman Spectrosc.* **2018**, *49*, 1356–1363, DOI: 10.1002/jrs.5377.
- (37) Fan, Q.; Chen, X.; Wei, L.; Yang, K.; Yu, C. The role of photoluminescence induced by  $\text{Yb}^{3+}/\text{Yb}^{2+}$  transformation in promoting the SPR effect in  $\text{Pd}/\text{Yb}^{3+}/\text{BiOBr}$  photocatalyst system. *Opt. Mater.* **2020**, *109*, No. 110316.
- (38) Yu, L.; Li, H.; Shang, H.; Xing, P.; Zhou, B.; Chen, Z.; Liu, X.; Zhang, H.; Shi, Y.; Zhang, L. Locally Asymmetric  $\text{BiOBr}$  for Efficient Exciton Dissociation and Selective  $\text{O}_2$  Activation toward Oxidative Coupling of Amines. *ACS Nano* **2023**, *17* (15), 15077–15084, DOI: 10.1021/acsnano.3c04268.



- (39) Li, J.; Sun, S.; Qian, C.; He, L.; Chen, K. K.; Zhang, T.; Chen, Z.; Ye, M. The role of adsorption in photocatalytic degradation of ibuprofen under visible light irradiation by BiOBr microspheres. *Chem. Eng. J.* **2016**, *297*, 139–147, DOI: 10.1016/j.cej.2016.03.145.
- (40) Yusoff, M. A. M.; Imam, S. S.; Shah, I.; Adnan, R. Photocatalytic activity of bismuth oxyiodide nanospheres and nanoplates in the degradation of ciprofloxacin under visible light. *Mater. Res. Express* **2019**, *6*, No. 0850g5.
- (41) Jiang, G.; Li, X.; Wei, Z.; Jiang, T.; Du, X.; Chen, W. Growth of N-doped BiOBr nanosheets on carbon fibers for photocatalytic degradation of organic pollutants under visible light irradiation. *Powder Technol.* **2014**, *260*, 84–89.
- (42) Hu, Q.; Sun, W.; Tao, R.; et al. Rational construction of tetraphenylporphyrin/bismuth oxybromide nanocomposite with accelerated interfacial charge transfer for promoted visible-light-driven degradation of antibiotics. *Res. Chem. Intermed.* **2022**, *48*, 235–250, DOI: 10.1007/s11164-021-04620-6.
- (43) (a) Cai, Z.; Zhong, J.; Li, L.; Jin, H. Oxygen vacancies enriched BiOBr with boosted photocatalytic behaviors. *Inorg. Chem. Commun.* **2021**, *126*, No. 108450. (b) Guo, F.; Chen, J.; Zhao, J.; Chen, Z.; Xia, D.; Zhan, Z.; Wang, Q. Z-scheme heterojunction g-C<sub>3</sub>N<sub>4</sub>@PDA/BiOBr with biomimetic polydopamine as electron transfer mediators for enhanced visible-light driven degradation of sulfamethoxazole. *Chem. Eng. J.* **2020**, *386*, No. 124014.
- (44) Tu, X.; Qian, S.; Chen, L.; Qu, L. The influence of Sn(II) doping on the photoinduced charge and photocatalytic properties of BiOBr microspheres. *J. Mater. Sci.* **2015**, *50*, 4312–4323, DOI: 10.1007/s10853-015-8983-3.
- (45) Lima, A. B.; Faria, E. O.; Montes, R. H. O.; Cunha, R. R.; Richter, E. M.; Munoz, R. A. A.; dos Santos, W. T. P. Electrochemical Oxidation of Ibuprofen and Its Voltammetric Determination at a Boron-Doped Diamond Electrode. *Electroanalysis* **2013**, *25* (7), 1585–1588, DOI: 10.1002/elan.201300014.
- (46) Švork, L.; Strežová, I.; Kianičková, K.; Stanković, D. M.; Otrisal, P.; Samphao, A. An advanced approach for electrochemical sensing of ibuprofen in pharmaceuticals and human urine samples using a bare boron-doped diamond electrode. *J. Electroanal. Chem.* **2018**, *822*, 144–152, DOI: 10.1016/j.jelechem.2018.05.026.
- (47) Yu, P. Y.; Cardona, M. Fundamentals of Semiconductors. In *Physics and Materials Properties*, 4th ed.; Springer: Heidelberg, Germany, 2010.
- (48) Falletta, E.; Longhi, M.; Di Michele, A.; Boffito, D. C.; Bianchi, C. L. Floatable graphitic carbon nitride/alginate beads for the photodegradation of organic pollutants under solar light irradiation. *J. Cleaner Prod.* **2022**, *371*, No. 133641.
- (49) Paustian, D.; Franke, M.; Stelter, M.; Braeutigam, P. Sonophotocatalysis—Limits and Possibilities for Synergistic Effects. *Catalysts* **2022**, *12* (7), No. 754, DOI: 10.3390/catal12070754.
- (50) Fazli, A.; Zakeri, F.; Khataee, A.; Orooji, Y. A BaTiO<sub>3</sub>/WS<sub>2</sub> composite for piezo-photocatalytic persulfate activation and ofloxacin degradation. *Commun. Chem.* **2022**, *5*, No. 95.
- (51) Jallouli, N.; Pastrana-Martínez, L. M.; Ribeiro, A. R.; Moreira, N. F. F.; Faria, J. L.; Hentati, O.; Silva, A. M. T.; Ksibi, M. Heterogeneous photocatalytic degradation of ibuprofen in ultrapure water, municipal and pharmaceutical industry wastewaters using a TiO<sub>2</sub>/UV-LED system. *Chem. Eng. J.* **2018**, *334*, 976–984, DOI: 10.1016/j.cej.2017.10.045.
- (52) Tanveer, M.; Guyer, G. T.; Abbas, G. Photocatalytic degradation of ibuprofen in water using TiO<sub>2</sub> and ZnO under artificial UV and solar irradiation. *Water Environ. Res.* **2019**, *91*, 822–829, DOI: 10.1002/wer.1104.
- (53) Chaker, H.; Fourmentin, S.; Chérif-Aouali, L. Efficient Photocatalytic Degradation of Ibuprofen under Visible Light Irradiation Using Silver and Cerium Co-Doped Mesoporous TiO<sub>2</sub>. *ChemistrySelect* **2020**, *5*, 11787–11796, DOI: 10.1002/slct.202002730.
- (54) Li, L.; Boda, M. A.; Chen, C.; Wang, F.; Liu, Y.; Yi, Z. BiOBr Micro-Nanosheets: Controllable Synthesis and Piezoelectric and Photoelectric Properties. *Cryst. Growth Des.* **2021**, *21* (12), 7179–7185, DOI: 10.1021/acs.cgd.1c01026.
- (55) Hu, J.; Chen, Y.; Zhou, Y.; Zeng, L.; Huang, Y.; Lan, S.; Zhu, M. Piezo-enhanced charge carrier separation over plasmonic Au-BiOBr for piezo-photocatalytic carbamazepine removal. *Appl. Catal., B* **2022**, *311*, No. 121369.
- (56) Miranda, M. O.; Cavalcanti, W. E. C.; Barbosa, F. F.; de Sousa, J. A.; da Silva, F. I.; Pergher, S. B. C.; Braga, T. P. Photocatalytic degradation of ibuprofen using titanium oxide: insights into the mechanism and preferential attack of radicals. *RSC Adv.* **2021**, *11*, 27720–27733, DOI: 10.1039/D1RA04340D.
- (57) Galloni, M. G.; Cerrato, G.; Giordana, A.; Falletta, E.; Bianchi, C. L. Sustainable Solar Light Photodegradation of Diclofenac by Nano- and Micro-Sized SrTiO<sub>3</sub>. *Catalysts* **2022**, *12* (8), No. 804, DOI: 10.3390/catal12080804.
- (58) Huang, W.; Hua, X.; Zhao, Y.; Li, K.; Tang, L.; Zhou, M.; Cai, Z. Enhancement of visible-light-driven photocatalytic performance of BiOBr nanosheets by Co<sup>2+</sup> doping. *J. Mater. Sci.: Mater. Electron.* **2019**, *30*, 14967–14976, DOI: 10.1007/s10854-019-01869-x.
- (59) Rimoldi, L.; Meroni, D.; Falletta, E.; Pifferi, V.; Falcioni, L.; Cappelletti, G.; Ardizzone, S. Emerging pollutant mixture mineralization by TiO<sub>2</sub> photocatalysts. The role of the water medium. *Photochem. Photobiol. Sci.* **2017**, *16*, 60–66, DOI: 10.1039/c6pp00214e.
- (60) Meroni, D.; Jimenez-Salcedo, M.; Falletta, E.; Bresolin, B. M.; Kait, C. F.; Boffito, D. C.; Bianchi, C. L.; Pirola, C. Sonophotocatalytic degradation of sodium diclofenac using low power ultrasound and micro sized TiO<sub>2</sub>. *Ultrason. Sonochem.* **2020**, *67*, No. 105123.